

## Full length article

## Enhanced resistance to helium irradiations through unusual interaction between high-entropy-alloy and helium



Tao Cheng<sup>a,1</sup>, Guo Wei<sup>a,1</sup>, Shengming Jiang<sup>b</sup>, Jian Zhang<sup>b,\*</sup>, Yongqiang Wang<sup>c</sup>, Peng Liu<sup>d,\*</sup>, Mengqing Hong<sup>a</sup>, Enkai Guo<sup>a</sup>, Fen Zhong<sup>a</sup>, Guangxu Cai<sup>a</sup>, Changzhong Jiang<sup>a</sup>, Feng Ren<sup>a,\*</sup>

<sup>a</sup> School of Physics and Technology, Center for Ion Beam Application, Hubei Nuclear Solid Physics Key Laboratory and MOE Key Laboratory of Artificial Micro- and Nano-Structures, Wuhan University, Wuhan 430072, China

<sup>b</sup> College of Energy, Xiamen University, Xiamen, Fujian, China

<sup>c</sup> Materials Science and Technology Division, Los Alamos National Laboratory, Los Alamos, NM 87545, USA

<sup>d</sup> Institute of Frontier and Interdisciplinary Science and Key Laboratory of Particle Physics and Particle Irradiation (MOE), Shandong University, Qingdao, Shandong 266237, China

## ARTICLE INFO

## Keywords:

High-entropy alloys  
In-situ irradiation  
MD simulation  
He bubble  
Nanochannels

## ABSTRACT

Finding high performance plasma-facing materials (PFMs) is one of the most important and challenging tasks for realizing the commercial application of fusion reactors. Herein, we found the CrMoTaWV high entropy alloy (HEA) is highly resistant to low-energy and high-flux He plasma exposure. The nanochannel HEA film has 20 times higher initial fluence for the formation of fuzz and a remarkable 8.9 times slower fuzz growth rate than those of W. Combining the *in-situ* TEM observation and the Molecular dynamics (MD) simulation of the He bubble growth process, a new mechanism for the enhanced radiation resistance in HEA with the unusual interaction between HEA and He is found, where, differing from traditional metal, bubble growth in HEA leads to non-directional emission of interstitial atoms while HEA greatly suppress the growth of He bubbles. The special nanochannel structure further rise the radiation resistance through releasing He out of the HEA film and reducing the He concentration. This new nanochannel refractory HEA material presents a promising choice as the PFMs with excellent performance and a much longer serving lifetime for future commercial fusion reactors.

## 1. Introduction

Nuclear energy, as clean, reliable, sustainable and affordable energy, is considered to be one of the most effective ways to solve the energy crisis and is crucial to worldwide economic prosperity and stability. Developing advanced nuclear material is the most important key point for the next generation of nuclear systems. Because helium (He) hardly dissolves in solids, He bubbles formed by the aggregation of transmuted or incident He atoms is one of the most serious and typical issues for nuclear materials, which greatly affects their microstructure and mechanical properties (e.g. swelling, hardening and embrittlement behaviors) [1,2]. Controlling the behavior of He atoms and their aggregates in materials is a key task for developing advanced nuclear materials. For example, developing high-performance plasma-facing materials (PFMs) is the most urgent challengeable task in the field of material for the realization of commercial fusion reactors because PFM

suffers from harsh environments, including irradiation by high fluxes of hydrogen isotopes (D and T) and He plasma ( $\sim 10^{22} \text{ m}^{-2}\text{s}^{-1}$ ) [3,4]. Tungsten (W) is considered as one of the most promising PFM due to its excellent physical and chemical properties, which was selected as the PFM for International Thermonuclear Experimental Reactor (ITER) [5–7]. Unfortunately, under the low-energy and high-flux He plasma exposure, microstructures, such as pinholes, craters or even fuzz, have been observed quickly on the W surface due to the rupture of bubbles and directional emission of W atoms to the surface [8,9], which not only affect the thermodynamic properties and lifetime of W, but also affect the stable operation of plasma.

To solve the issue of the He bubble in nuclear materials, different strategies are applied. Taking the PFMs as an example, one strategy is to tailor the structure of W, such as ultrafine-grained W, nano-porous and nanochannel W [10–13]. The introduction of a large number of grain boundaries reduces the local concentration of He atoms in the matrix by

\* Corresponding authors.

E-mail addresses: [zhangjian@xmu.edu.cn](mailto:zhangjian@xmu.edu.cn) (J. Zhang), [pengliu@sdu.edu.cn](mailto:pengliu@sdu.edu.cn) (P. Liu), [fren@whu.edu.cn](mailto:fren@whu.edu.cn) (F. Ren).

<sup>1</sup> These authors contributed equally to this work.

absorbing He atoms. Compared with the limitation of grain boundaries in absorbing He bubbles, nanochannel structure can release absorbed He atoms to the outside of the matrix to greatly reduce He concentration [13]. Another strategy for developing high-performance PFM is to tailor the elemental composition of W to inhibit the growth of He bubbles to large ones through reducing the diffusion of He atoms. W-based binary alloys such as W-Re [14,15], W-Ti [16,17], W-Ta [18,19] and W-Cr [20,21] show enhanced radiation-resistance.

Recently, a novel class of multi-principal elemental alloys, composed of four or five elements in a quasi-equal atomic ratio, also named high entropy alloys (HEAs), has been developed. Compared with traditional materials, HEAs exhibit excellent mechanical properties, such as improved wear-resisting, strength, hardness and oxidation resistance [22–26]. These excellent properties are closely related to the lattice distortion effect in structure and the "cocktail" effect in properties [27–31]. Based on its unique structure, many studies have demonstrated the excellent irradiation resistance of HEAs to neutron irradiation [32–34]. The systematical study by Lu et al. on the nickel ion ( $\text{Ni}^+$ ) irradiation of Ni and a series of Ni-based middle and high entropy alloys at 500 °C indicated the significant inhibitory effect of HEA on the formation of voids [35]. Chen et al. found that the He bubble size in the NiCoFeCr HEA was smaller than that in the Ni under  $\text{He}^+$  ion irradiation at 673 K [36]. However, the interplay between HEA and He bubbles, meaning the influence of interaction between He bubble growth and the microstructure of HEA to each other, is unclear. Meanwhile, the study on the formation and growth of fuzz structure in HEA and the possibility of the application of HEAs as PFMs under the environment of high-flux He plasma irradiation has not been studied.

In this work, combining the advantages of both the nanochannel structure and high entropy alloys, a new nanochannel CrMoTaWV HEA is designed, prepared and tested under the irradiation of high-flux He plasma at high temperature. The results show that the nanochannel HEA film has 20 times higher initial fluence for the formation of fuzz and a remarkable 8.9 times slower fuzz growth rate than those of W during He plasma irradiation. A new mechanism for the greatly enhanced resistance of HEA compared to traditional metal to He irradiations through the unusual interaction between the HEA and He is proposed by the *in-situ* TEM observation and molecular dynamics simulations of the growth of He bubble, where the bubble growth leads to non-directional emission of interstitial atoms while HEA greatly suppress the growth of He bubbles. The presented results show that the refractory metal HEA is a kind of promising PFM and nuclear structural materials with high performance and enhanced serving lifetime.

## 2. Experimental procedures

### 2.1. Materials preparation

The CrMoTaWV nanochannel HEA film was deposited on polished silicon (100) wafers and W substrates at 873 K by ultrahigh vacuum DC magnetron sputtering (ULVAC, ACS-4000-C4). The sputtering target with equal-molar ratio composition was prepared by powder metallurgy by uniformly mixing W, Ta, Mo, Cr and V with high purity (>99.99%) in argon atmosphere, which also was used as a contrast sample, bulk HEA (the sizes of grains are about 20–50  $\mu\text{m}$  shown in Fig. S1a). Cr, Mo, Ta, W and V were selected due to their high melting point and high solid solubility of each other. The power was set to 150 Watts, and the working pressure was maintained at 0.6 Pa, which was named the nanochannel HEA film. The W film was prepared by ultrahigh vacuum DC magnetron sputtering deposition with the power of 150 W and the pressure of 0.6 Pa. All the films grew to a thickness of about 1  $\mu\text{m}$ . As contrast samples, the bulk HEA and bulk W were mechanically polished into a mirror and then cleaned with acetone ultrasonic. Bulk W (the sizes of grains are about 5–10  $\mu\text{m}$  shown in Fig. S1b) (99.95 wt% purity) was commercial polycrystalline W produced by ATTL Advanced Materials Co., Ltd. Beijing, China.

### 2.2. He plasma irradiation

To investigate the radiation resistance of the nanochannel HEA film to plasma, the low-energy and high-flux He plasma exposure was performed by the large-power inductively coupled plasma (ICP) irradiation system at Dalian University of Technology [37]. During  $\text{He}^+$  plasma exposure, targets were biased to -30 V to facilitate energetic-ion bombardment of the flux  $\Gamma \sim 1.1 \times 10^{22} \text{ ions m}^{-2}\text{s}^{-1}$ . Taking account of the plasma potential of 20 V, the energy of impacting He ions is 50 eV. The sample surface temperature is  $1270 \pm 30$  K, measured by an infrared STL200-A620 pyrometer. The  $\text{He}^+$  ions fluence is 0.1, 0.5, 1, 5, 10 and  $30 \times 10^{25} \text{ ions m}^{-2}$ , respectively.

### 2.3. In-situ $\text{He}^+$ irradiation

To investigate the evolution of He in nanochannel HEA, the *in-situ*  $\text{He}^+$  irradiation was performed within the Xiamen Multiple Ion Beam *In-situ* TEM Analysis Facility (XIAMEN Facility) at Xiamen University [38]. XIAMEN Facility consists of a TECNAI G20 F30 TWIN TEM coupled to a 400 kV implanter (30–400 kV) and a 50 kV hydrogen/helium coaxial ion source (10–50 kV). The nanochannel HEA and W films in the TEM sample holder were irradiated by 30 keV  $\text{He}^+$  ions. The sample temperature was 1123 K and was controlled by a Gatan 652 double-tilt heating holder with a water-cooling system. The ion flux was approximately  $4.0 \times 10^{13} \text{ He}^+ \text{ ions cm}^{-2}\text{s}^{-1}$ , and the total irradiation time was 110 min. The thickness of the *in-situ* monitored region for the nanochannel HEA film and the W film was about 65 and 50 nm, respectively, which was estimated based on the energy-filtered imaging by the log-ratio method (SI Appendix, Fig. S2) [39,40]. TEM images with the under-focus value of -700 nm were captured by —TECNAI G20 F30 TWIN TEM operating at 300 kV. The displacement per atom (dpa) and the He concentration of both the HEA and W samples were calculated by SRIM-2013 in "Quick Kinchin-Pease" mode (Fig. S3). The threshold displacement energy of W, Ta, Mo, Cr, and V atoms were 90, 90, 60, 40, and 40 eV, respectively [41]. Therefore, according to the measured thickness, the injected He concentration rates in the nanochannel HEA and the W films were approximately  $1.07 \times 10^{13}$  and  $0.99 \times 10^{13} \text{ He}^+ \text{ ions cm}^{-2}\text{s}^{-1}$ , respectively.

### 2.4. Molecular dynamics (MD) simulation and calculation processes

The LAMMPS code [42] was used to perform all MD simulations and molecular statics (MS) calculations. In previous studies, Zhou et al. developed an integrated EAM potential database applicable to many metals and their alloys [43]. Due to its simplicity and consistency among different elements, this set of EAM parameters has been extensively used to simulate the properties of HEAs [44–46]. Thus, in this work, the embedded atom method (EAM) potential for elements (Mo, Ta, W) was taken from Zhou et al. [43]. The interatomic potential of Cr was taken by Lin et al. [47], and the interatomic potential of V was taken by Zhao et al. [44]. The parameter models of Cr and V are the same as Zhou et al. The He-He interactions were described by Beck potential [48]. However, there is no better interaction potential of He atoms in HEA. The interactions between He and HEA were used by the ZBL potential. Peng and Liu et al. has used ZBL potential to describe the interaction potential between Fe, C and He, and successfully explored the evolution of He in Fe/C materials [49]. Based on the test simulation of the ZBL potential in Supplementary Note 1, we confirm that the ZBL potential used here is sufficient to simulate the growth of He bubbles in HEA.

The HEA model was generated by randomizing the elements on the lattice sites. We constructed 10,000 models using this random substitution method and selected the lowest energy configuration for subsequent MD simulations, as it is difficult to obtain a stable configuration with a small number of random substitutions. The lattice parameter of CrMoTaWV (BCC) was calculated from the minimum value of the energy-volume curve, which is 3.141 Å, almost the same as the value

measured in our experiment ( $3.165 \text{ \AA}$ ). The parameters of the HEA model are given in Fig. S4. A simulation model of  $40a_0 \times 40a_0 \times 40a_0$ , (where  $a_0$  is the lattice constant of HEA) containing 128,000 atoms was built. The X, Y and Z directions of the simulation box are [100], [010] and [001], respectively, and all periodic boundary conditions are used in all directions. The growth processes of He bubbles in the HEA was same as the W described in *Supplementary Note 1*.

### 2.5. Characterization methods

The surface and cross-sectional morphologies of the samples were examined by a scanning electron microscope (Hitachi S-4800). The cross-sectional transmission electron microscopy (TEM) was performed using a JEOL JEM-2100 microscope operating at 200 kV. The TEM samples were prepared by focus ions beam (FIB) and traditional processes including mechanical grinding, polishing, dimpling and ion milling. The He desorption behaviors in the nanochannel HEA and W films were analyzed by thermal desorption spectroscopy (TDS). The sample was heated to 1000 K at a constant rate of  $0.5 \text{ K s}^{-1}$  in an ultra-high vacuum chamber, and the He desorption rate was measured by quadrupole mass spectrometer (Pfeiffer Vacuum, QME 220). The temperature was measured using a sheathed type K Omega thermocouple that directly contacted the sample surface. The retention of He atoms in the irradiated samples was measured by elastic recoil detection (ERD) using a 12 MeV  $^{12}\text{C}^{3+}$  analyzing beam.

## 3. Results

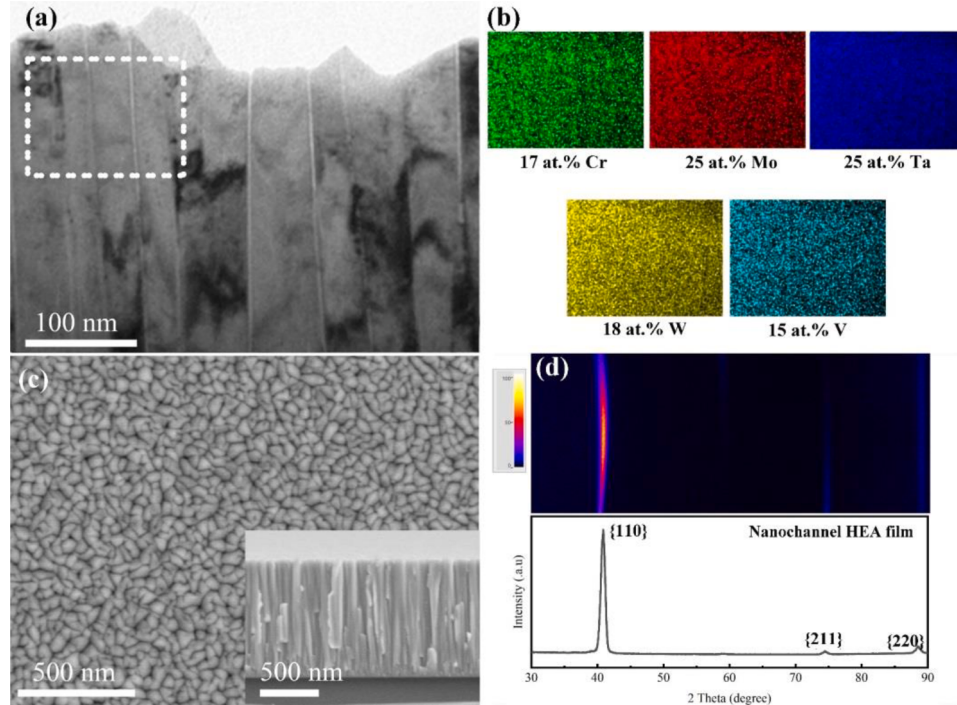
### 3.1. Microstructure of nanochannel HEA film

Fig. 1a and 1c show the TEM and SEM images of the CrMoTaWV nanochannel HEA film, where the nanochannels are formed between the HEA nanocrystalline columns. The EDS mapping (Fig. 1b) of the area in the white box in the cross-sectional TEM image shows the uniform distributions of Cr, Mo, Ta, W, and V elements and the corresponding

atomic percentages are 17, 25, 25, 18, and 15, respectively. The 2D grazing-incidence XRD pattern (Fig. 1d) indicates that the nanochannel HEA film is a single-phase body-centered cubic (bcc) structure with the preferred growth in the [110] direction.

### 3.2. Low-energy He plasma exposure

To evaluate the resistance ability of HEA to plasma irradiation, the nanochannel HEA film, the bulk HEA and bulk W were exposed to the low-energy and high-flux He plasma. Fig. 2 shows the surface morphology SEM images and corresponding cross-sectional SEM and TEM images of the bulk W, bulk HEA and the nanochannel HEA film irradiated by He plasma to the fluences from  $1 \times 10^{24}$  to  $3 \times 10^{26} \text{ ions m}^{-2}$ . Except for some pinhole structures, no change is observed on the surface of the nanocrystalline columns in the nanochannel HEA film irradiated to the fluence of  $1 \times 10^{25} \text{ ions m}^{-2}$ . In the corresponding cross-sectional SEM image (Fig. 2b1), no obvious damage is observed on the top surface of the columns. When the fluence increases to  $5 \times 10^{25} \text{ ions m}^{-2}$ , the top layer of the nanocrystalline column is damaged and evolves towards the nano-porous structure, leaving a rough surface. As the fluence continuously increases to  $1 \times 10^{26} \text{ ions m}^{-2}$ , a typical fuzz nanostructure is gradually formed on the surface of the nanochannel HEA film. The corresponding cross-sectional SEM image shows a thin layer of fuzz with a thickness of 120 nm. The fuzz layer further grows to about 250 nm at the highest fluence of  $3 \times 10^{26} \text{ ions m}^{-2}$  (Fig. 2a4 and 2b4). However, a nano-porous structure appears on the surface of the bulk HEA and begins to evolve toward fuzz at the fluence of  $1 \times 10^{25} \text{ ions m}^{-2}$ . When the fluence increases to  $5 \times 10^{25} \text{ ions m}^{-2}$ , the fuzz layer is formed on the surface (Fig. 2d2), and the fuzz continuously increases to 400 and 600 nm with the increase of the fluences to  $1 \times 10^{26}$  and  $3 \times 10^{26} \text{ ions m}^{-2}$ . For comparison, a nano-porous structure appears on the W surface at the lowest fluence of  $1 \times 10^{24} \text{ ions m}^{-2}$ , and a fuzz layer with a thickness of 160 nm has appeared after being irradiated to  $5 \times 10^{24} \text{ ions m}^{-2}$ . Further increasing the fluence to  $3 \times 10^{26} \text{ ions m}^{-2}$ , the thickness of the fuzz layer rapidly increases to 2.5  $\mu\text{m}$ , which is about 10



**Fig. 1.** Microstructure of the nanochannel HEA film. (a) Cross-sectional TEM image of the CrMoTaWV nanochannel HEA film; (b) EDS element mapping images from the white box area in (a); (c) surface SEM image of the nanochannel HEA film, and the corresponding cross-sectional SEM image; (d) 2D grazing-incidence XRD patterns of the nanochannel HEA film.

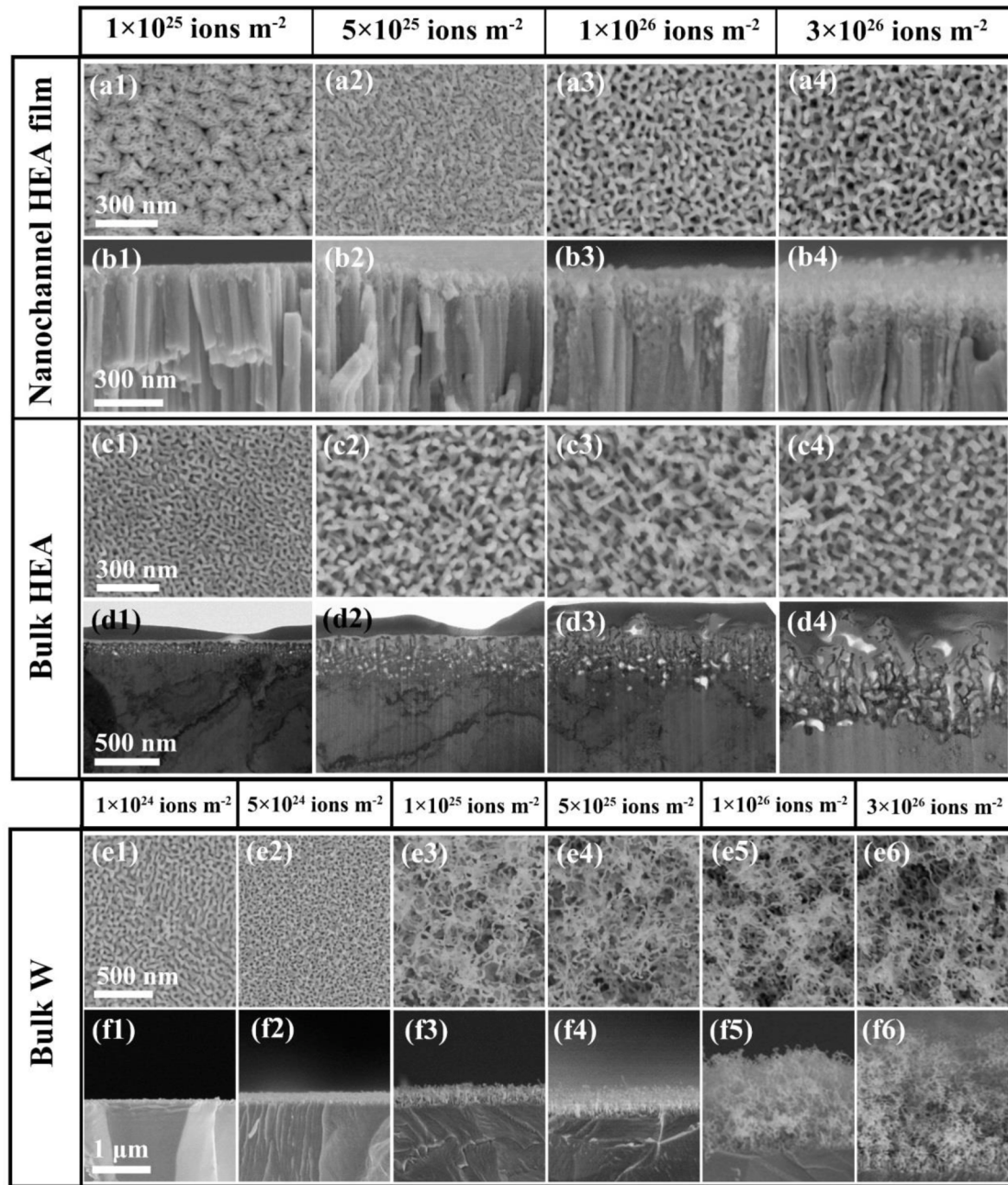


**Fig. 2.** Surface morphology SEM images and corresponding cross-sectional SEM and TEM images of the samples irradiated by He plasma to fluences from  $1 \times 10^{24}$  to  $3 \times 10^{26} \text{ ions m}^{-2}$ . (a1-a4, b1-b4) the nanochannel HEA films, (c1-c4, d1-d4) bulk HEA, (e1-e6, f1-f6) bulk W. The scale bars in (a1-a4), (b1-b4), (c1-c4), (d1-d4), (e1-e6) and (f1-f6) are same, respectively.

times of that of the nanochannel HEA film irradiated to the same fluence. Therefore, in general, the bulk HEA has a much better ability than the bulk W in improving the initial fluence for the formation of fuzz and slowing down the growth of fuzz under the He plasma irradiation. The nanochannel HEA with abundant free surface further enhances its radiation resistance.

Table S1 shows the thicknesses of the fuzz layer on various W grades under similar He plasma irradiation [11,13,50,51]. The thickness of fuzz in the commercial W, nanochannel W film, La<sub>2</sub>O<sub>3</sub>-doped W or ultrafine-grained W is up to microns at the fluences of  $3 \sim 4 \times 10^{26} \text{ ions m}^{-2}$ , which is much larger than that of the nanochannel HEA film. More quantitatively, the expression of fuzz thickness ( $\chi$ ) depending on He fluence ( $\Phi$ ) is used according to [52]:

$$\chi(\Phi) = (C(\Phi - \Phi_0))^{1/2} \quad (1)$$

where  $C = 2D/\Gamma$  with  $\Gamma$  is the ion flux and D is a quantity akin to a Fick effective diffusion coefficient,  $\Phi (= \Gamma t)$  is the irradiation fluence and  $\Phi_0$  is an initial He fluence required for the formation of fuzz morphology. Here,  $(2D/t)^{1/2}$  can be regarded as the growth rate of fuzz [53]. The  $t^{1/2}$  dependence of fuzz thickness suggests that the fuzz growth process is dominated by diffusion and the growth kinetics is consistent with one dimensional-diffusional transport [50], where the adatoms induced by He<sup>+</sup> ion bombardment diffuse along the sides of tendrils (fuzz) to their tips, leading to the growth of fuzz structure [54]. The quantitative measurement of the pure growth of fuzz is difficult, because the actual thickness of fuzz is affected by many factors, e.g. the thickness

of fuzz (porous ratio), the erosion (or surface sputtering), re-deposition and annealing (fuzz re-integration within the bulk/substrate) effects [55,56]. In this work, we used steady-state He plasma irradiation at 1270 K, the re-deposition and annealing effects can be ignored. It should be noted that real D is also time dependent if considering erosion, re-deposition and annealing effects. The fuzz layer thickness in Table S1 is plotted as a function of He ion fluence in Fig. 3. The fuzz thicknesses are fitted well with Eq. (1) and the effective diffusion coefficients (D) obtained are  $1.12 \times 10^{-12}$ ,  $7.58 \times 10^{-14}$  and  $1.41 \times 10^{-14} \text{ cm}^2 \text{ s}^{-1}$  for the bulk W, bulk HEA and nanochannel HEA film, respectively. For a given irradiation time,  $(2D)^{1/2}$  can be regarded as an average growth rate. Therefore, the growth rate of fuzz in the bulk HEA is 3.8 times lower than that of the bulk W. Furthermore, the growth rate of fuzz in the nanochannel HEA films is remarkably 8.9 and 2.3 times lower than those of the bulk W and bulk HEA, which means it has much a longer lifetime as a PFM resistant to He plasma irradiation. The  $t^{1/2}$  dependence nature of fuzz growth on the bulk and the nanochannel HEA indicates that the growth mechanisms of these two materials also are diffusion limited. To understand the unusual ability of HEA to resist He plasma irradiation, it will be analyzed from the experimental *in-situ* TEM observation and the theoretical MD simulation of He bubble growth processes in these two materials.

### 3.3. *In-situ* $\text{He}^+$ ions irradiation

The above results indicate that the growth of the He bubble leads to the different changes in microstructure and morphology in HEA and W. Thus, the size of He bubbles can greatly affect the formation and growth of fuzz structure. Conversely, it should be noted that the intrinsic characteristics of materials may act on the behavior of He. To further understand the reasons for the better resistance to He plasma irradiation in HEA, the influence of substrates (the nanochannel HEA and W film) on the growth and evolution of He bubbles was observed directly from the TEM during *in-situ*  $\text{He}^+$  ions irradiation. Here, the *in-situ* irradiation of the nanochannel HEA and W films was done by 30 keV  $\text{He}^+$  ions at 1123 K to the highest fluence of  $7.07 \times 10^{16} \text{ ions m}^{-2}$ . The TEM monitored the evolution of He bubbles in the nanochannel HEA and W films during *in-situ* irradiation to a series of fluences is shown in Fig. 4a–4j. Unlike the clear He bubbles in the W film, the He bubbles in the nanochannel HEA film are not obvious because of their small size. Moreover, the initial fluence for the formation of He bubbles in the nanochannel HEA film was  $1.41 \times 10^{16} \text{ ions m}^{-2}$ , which was 2 times higher than that of  $6.52 \times 10^{15} \text{ ions m}^{-2}$  for the W film. The He bubble density and size in the nanochannel HEA film and the W film irradiated to the different fluences are statistically shown in Fig. 4k and 4l. The nanochannel HEA film has a higher density of He bubbles at the initial

fluence of He bubble formation, and the density changes little with the increase of the fluence. However, the bubble density in the W film increases rapidly with the fluence until it reaches a peak and then decreases, while the size of He bubbles remains almost constant and then increases quickly before the fluence is higher than  $3.26 \times 10^{16} \text{ ions m}^{-2}$ .

Obviously, the influence of HEA and W on the evolution of the He bubble is quite different. In the W film, it consists of two stages, the rapid nucleation and ripening of He bubbles, similar to those of other metals [57,58]. For injected He atoms in the W matrix, there is a strong repulsive potential between W-He, while the repulsive potential between He-He is weaker [59]. Therefore, free He atoms gather into He clusters due to their relatively rapid diffusion, which continuously absorbs He atoms to form visible He bubbles even at a low irradiation fluence. With the increase of irradiation fluence to  $3.26 \times 10^{16} \text{ ions m}^{-2}$ , the decrease of bubble density in W film means the migration and coalescence (MC) of He bubbles (Fig. S5) [60]. However, the He bubbles of the nanochannel HEA film is difficult to grow through the MC mechanism with the increase of the fluence (corresponding to no obvious change in bubble density). Different from W, HEA has complex surrounding environments for interstitial He atoms due to different chemical element substitution. The difference in atomic radius of the element results in the lattice distortion in the HEA, hindering the diffusion of He atoms and delaying nucleation and growth of He bubbles [61]. El-Atwani et al. reported that the migration energy of He in Cr-V-Ta-W HEA was 2 times larger than that in W [62]. Hence, due to the easier trapping of He atoms at lattice distortions and the lower diffusion rate of He atoms, the appearance of the small He bubbles in HEA needs higher irradiation fluence than that of W, which means the growth of He bubbles in HEA is much slower than in W.

Fig. 4m shows the He desorption spectra with the increase of temperature in the nanochannel HEA film and the W film irradiated by 40 keV  $\text{He}^+$  ions to the fluence of  $1 \times 10^{17} \text{ ions m}^{-2}$ . TDS spectra can be ascribed to adsorption sites characterized by activation energy for desorption of different forms of He in materials [63]. Compared with the two desorption peaks observed in the W film, only one desorption peak appears in the nanochannel HEA film before 1000 K. The desorption peaks at the 650 and 980 K in the W film are attributed to He de-trapping from a vacancy ( $\text{He}_\text{V}$ ) and dislocation loops near-surface [64]. Therefore, the first desorption peak at 840 K in the nanochannel HEA film is inferred to be the desorption from  $\text{He}_\text{V}$  clusters. The higher desorption temperature of He in the nanochannel HEA film means a stronger trap for He atoms in trapping sites. Compared with the W film, He atoms are more difficult to desorb from  $\text{He}_\text{V}$  clusters in the nanochannel HEA film, which can hinder the coalescence of small He bubbles. It is consistent with the *in-situ* TEM observation that the density of smaller He bubbles in HEA remains almost constant.

### 3.4. MD simulation of He bubbles growth

Molecular dynamics simulation is further carried out to study the mechanism for suppressing the growth of fuzz and the influence of He bubble evolution on HEA microstructure. The growth process of He bubbles in HEA is simulated by MD with the ZBL potential for the first time. Fig. 5a shows the simulated pressure evolution of a He bubble in the HEA as a function of simulation time or the growth of the He bubble. The pressure curve in the HEA appears a smooth downward trend, which is different from the evolution of the He bubble in pure W (SI Appendix, Fig. S6). The pressure of the He bubble in pure W dropped at 0.065 and 0.28 ns, which is due to the directional emission of self-interstitial atoms (SIAs) and dislocation loops as shown in the red atoms around the He bubble in the insert images (i and ii) of Fig. S6. While in the growth process of the He bubble in HEA, the smooth downward indicates that SIAs in HEA are continuously squeezed out the lattice sites. Oddly, SIAs are not emitted in the form of dislocation loops, but are distributed irregularly around the He bubble as shown in the insert images (i and ii) of Fig. 5a. To understand this different phenomenon, the evolution of

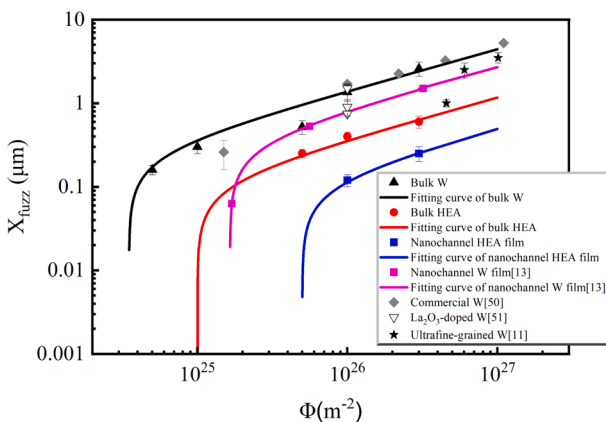
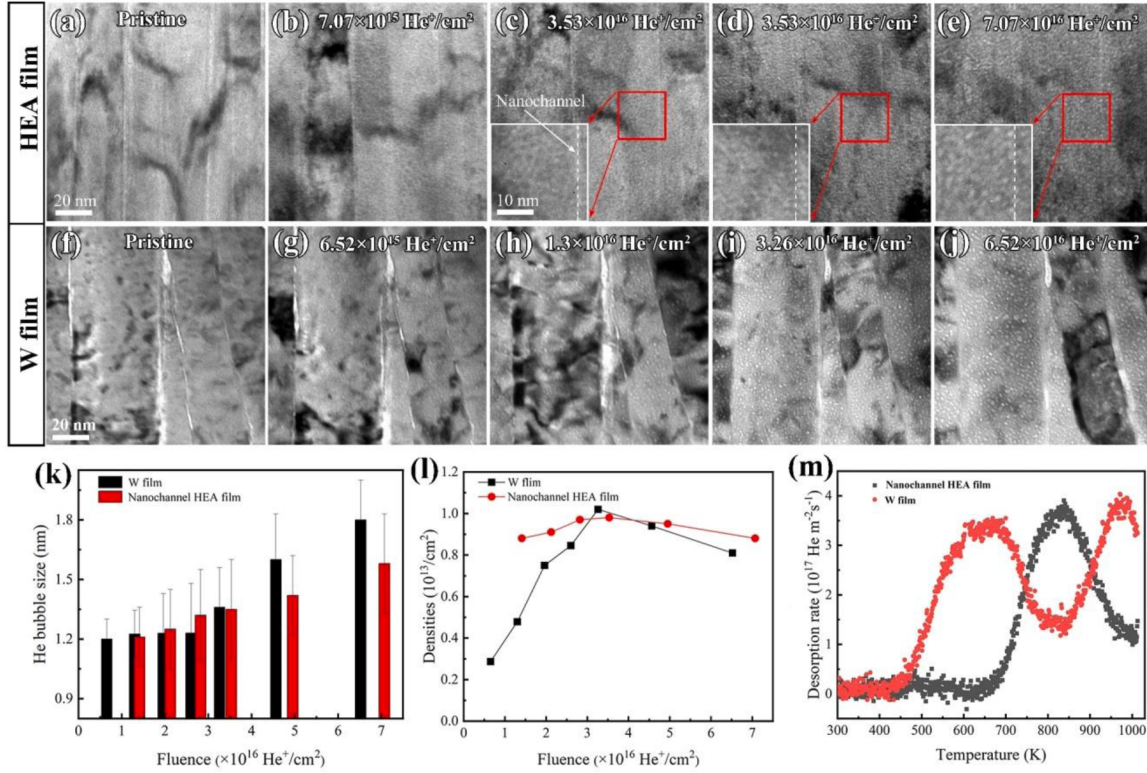


Fig. 3. Fuzz thickness of the nanochannel HEA film, bulk HEA, bulk W and the results in Refs. [11,13,50,51] and the corresponding fitting curves are plotted according to Eq. (1).



**Fig. 4.** *In-situ* bright-field TEM images of the He bubbles formation and evolution in the nanochannel HEA film (a–e) and W film (f–j) irradiated by 30 keV He<sup>+</sup> ions at 1123 K to the fluences of  $7.07 \times 10^{16} \text{ He}^+ \text{ cm}^{-2}$ . Insets in (c–e) show magnified images of the red box regions. The scale bar in (a–j) are the same (20 nm) and the inset images in (c–e) have the same scale bar (10 nm). (k) and (l) The size and density distributions of He bubbles in the nanochannel HEA film and W film during *in-situ* TEM irradiation, respectively. (m) The He desorption spectra of the nanochannel HEA film and the W film irradiated by 40 keV He<sup>+</sup> ions to the fluence of  $1 \times 10^{17} \text{ m}^{-2}$ .

SIAs in HEA was observed. Taking the  $\langle 111 \rangle$  dumbbell as an example, it can be found that the orientations and types of the SIAs after relaxing depend on local atomic environments. For example, the unrelaxed  $\langle 111 \rangle$  dumbbell of Cr was placed in the different locations of HEA in Fig. 5c, the  $\langle 111 \rangle$  dumbbell of Cr transferred to four types after relaxing, the  $\langle 110 \rangle$  dumbbell composed of other different atoms, the  $\langle 110 \rangle$  dumbbell of Cr, no change or the  $\langle 111 \rangle$  dumbbell composed of other different atoms. Moreover, the disorder of chemical elements results in the different local environments of each atom and further the different interstitial formation energy of each element at different positions. Fig. 5b shows the distributions of the interstitial formation energies of every element, which are lower than the formation energy of the interstitial W atom in pure W (9.70 eV). The statistics of the formation energy of each element at different positions in the system are shown in Fig. S7. Therefore, it is difficult to emit directionally dislocation loops in HEA during the growth of the He bubble due to complex atomic environments.

Furthermore, two simulation surface models of  $20a_0 \times 20a_0 \times 28a_0$  (where  $a_0$  is the lattice constant of HEA or W) were built based on the experiment of He plasma irradiation. The X, Y and Z directions of the simulation box are [100], [010] and [001], respectively. Periodic boundary conditions are used in the X and Y directions and the Z direction is the free surface (SI Appendix, Fig. S8). The growth process of the He bubble near the surface of HEA and W (25 Å from the surface) at 300 K were shown in Fig. 6. The emission of dislocation loops in W can be observed clearly from Fig. 6g, and a large number of W adsorbed atoms will accumulate on the surface with the growth of the He bubble, which is easy to form protrusions (Fig. 6h–6j). However, there is no emission of dislocation loops toward the surface in HEA, and there are only a few atoms on the surface lifted by He bubbles. When the number of He in the bubble reaches 800, the bubble is broken and most of He

atoms are released (Fig. 6e). At the same time, the surface of HEA keeps smooth except for the pinholes (SI Appendix, Fig. S9). While the He bubble with the same He number in W is remained because of the existence of directionally emitted W protrusion on its above surface. The non-directional emission of dislocation loops observed in HEA indicates the quite different response of HEA to the growth of the He bubble compared with W. At present, two synergistic factors affecting the rapid formation and growth of fuzz in W are generally accepted under high-flux He plasma irradiation [8,65–67]. One factor is the formation of the island-like protrusion on the surface. Another factor is the rupture of the He bubble near the surface. The above simulation results indicate that the HEA and its free surface can effectively suppress the formation and growth of fuzz structure, therefore having a great advantage in resistance to He plasma irradiation.

#### 4. Discussion

Combing the above simulation and experimental results, a new mechanism for the enhanced resistance to He<sup>+</sup> irradiation in HEA different from W through the unusual interaction between HEA and He is proposed as shown in Fig. 7f. For the influence of He bubble growth on the microstructure of materials, Fig. 7a–7d show the TEM images of the nanochannel HEA film irradiated to different fluences, which presents the microstructure evolution of the formation of fuzz during plasma irradiation. Due to the non-directional emission of interstitial atoms in the HEA, at the initial stage of fuzz formation, there is no protrusion appears on the surface although a large number of He bubbles accumulate beneath the surface (Figs. 6a–6c and 7a), which is an important factor in increasing the fluence of fuzz formation. With the increase of fluence, the He bubble near the surface will burst and form pinholes on the surface (Fig. S9). However, even though pinholes remain on the

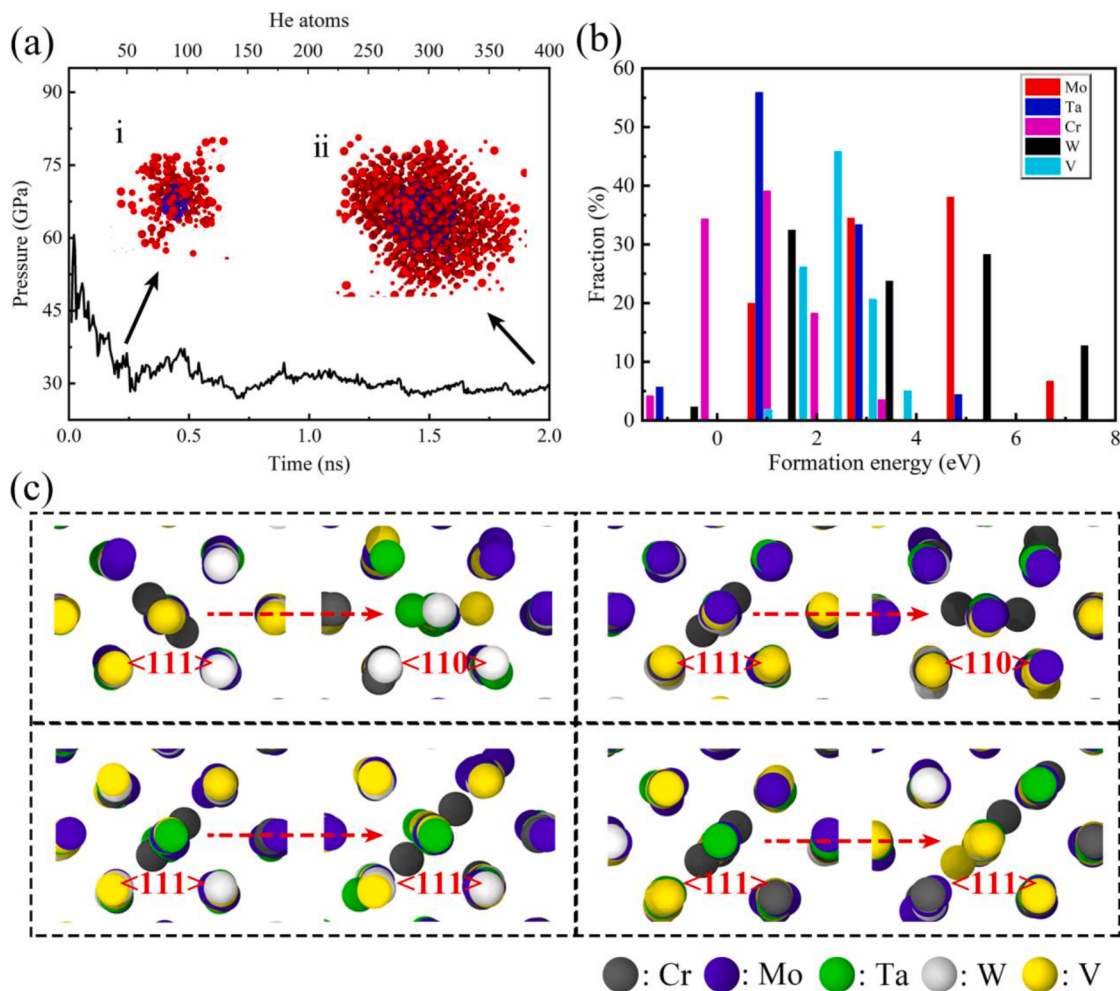


**Fig. 5.** The MD simulation of the He bubble growth in the HEA. (a) The pressure of He bubble in HEA as a function of simulation time (i.e. the number of He atoms); the inserts of i and ii in (a) show the positions of SIAs near the He bubble in the HEA at 0.13 and 2.0 ns; the red atoms are self-interstitial atoms, and the blue atoms are He atoms. (b) Formation energy distribution of self-interstitial atoms in the HEA. (c) Four types variation of the  $\langle 111 \rangle$  dumbbell of Cr before and after relaxed.

surface, no other obvious change in surface morphology was found shown in Fig. 2a1, indicating that no interstitial atom is emitted to the surface. However, W adatoms and protrusions introduced by He bubbles are rapidly formed on the surface of W, as shown in Fig. 7e. With the increasing number of He bubbles rupturing, the surface of HEA will gradually evolve towards the nanostructure, like the surface morphology in Fig. 2a2, and eventually form fuzz structure (Fig. 2a3 and 2a4). Therefore, the nanostructure is formed only by the rupture of He bubbles in the HEA, which greatly reduces the growth rate of fuzz. On the other hand, the *in-situ* TEM observation of  $\text{He}^+$  irradiation clearly shows that the inherent characteristics of HEA retroact to the behavior of He atoms and suppress the growth of He bubbles. With the lower formation energy of interstitial He in HEA than in W [62], there are many strong sinks or sites to trap He atoms, which disperses He in HEA and greatly reduces local He concentration. Therefore, under the same irradiation fluence, the bubble density in HEA is much higher than in W. Meanwhile, the higher migration energy of He in HEA blocks the diffusion of He, which further suppress the growth of the He bubble through coalescence even at a high temperature of 1123 K. Therefore, HEA with both low formation energy and high migration energy for He suppress the formation and growth of the He bubble, which further suppresses the formation and growth of fuzz structure and increase the radiation resistance. Thus, differing from traditional metal, the unusual interaction between HEA and He leads to the enhanced radiation resistance of HEA. Others, the XRD patterns of the nanochannel HEA

films irradiated by 40 keV  $\text{He}^+$  ions to the fluence of  $1 \times 10^{17}$  ions/ $\text{cm}^2$  at room temperature and 50 eV He plasma to the fluence of  $1 \times 10^{26}$  ions/ $\text{m}^2$  at 1270 K are given in Fig. S10, which shows that the phase structure of the nanochannel HEA films are stable under current irradiations.

Compared with the bulk HEA, the nanochannel HEA film has even better resistance to He plasma irradiation. One reason is that, according to the MD simulation shown in Fig. 6e, the free surface is easier to release He atoms from the He bubbles under the near-surface of HEA without changing its surface morphology. Meanwhile, the nanochannels in the film can absorb He atoms in the matrix and release them to the outside, reducing the concentration of He atoms in the matrix as the diagrammatic sketch shown in Fig. 7g. Elastic recoil detection (ERD) analysis shows that the relative concentration of He retained in the 40 keV  $\text{He}^+$  irradiated nanochannel HEA film (89.3%) at room temperature is less than that in the dense HEA film (95.3%) (SI Appendix, Figs. S11 and S12). It should be mentioned that, in our previous work, we found the relative concentration of He atoms retained in the nanochannel W film was lower at the higher irradiation fluence [13]. Therefore, it can be deduced that more He can be released through the nanochannels under high fluence He plasma irradiation at high temperature. The absence of large He bubbles near the nanochannels shown in Fig. 7d also indicates their ability in releasing He atoms. The release of He atoms from the nanochannels makes the He concentration in the nanochannel HEA film lower than that in the bulk HEA, which is also one of the important

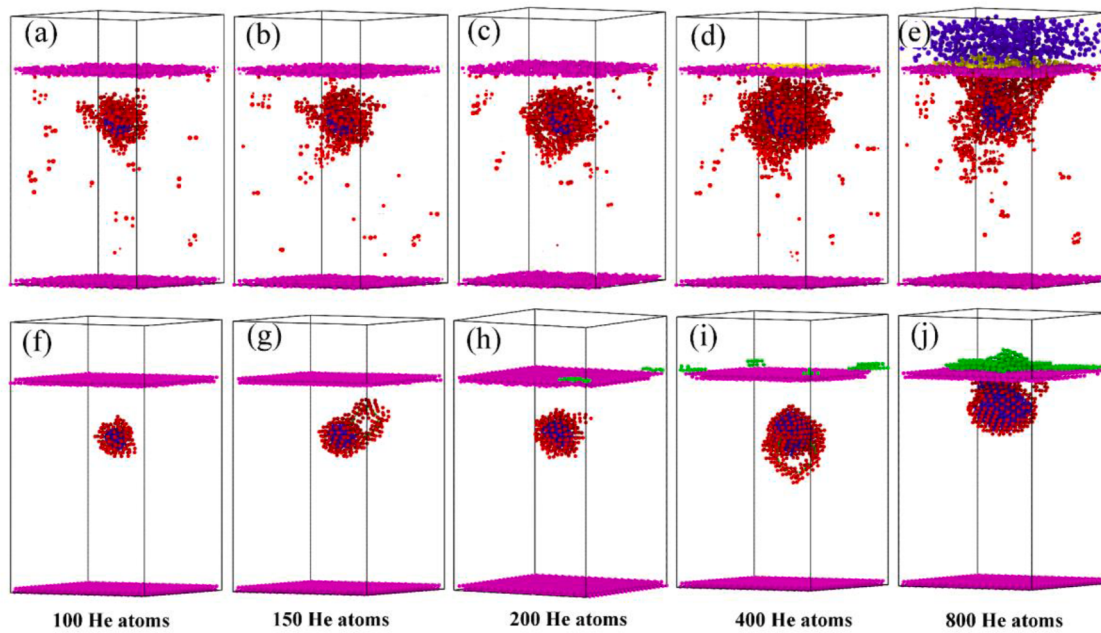


**Fig. 6.** He bubble growth process in the HEA (a–e) and W (f–j) close to the surface as the He atom numbers increase to 800 atoms at 300 K. The yellow atoms in (d) and (e) are the surface atoms that were lifted up by the He bubble before it burst; the blue atoms in the (e) are the released He atoms; the green atoms in the (g–j) are emitted W adatoms induced by He bubble.

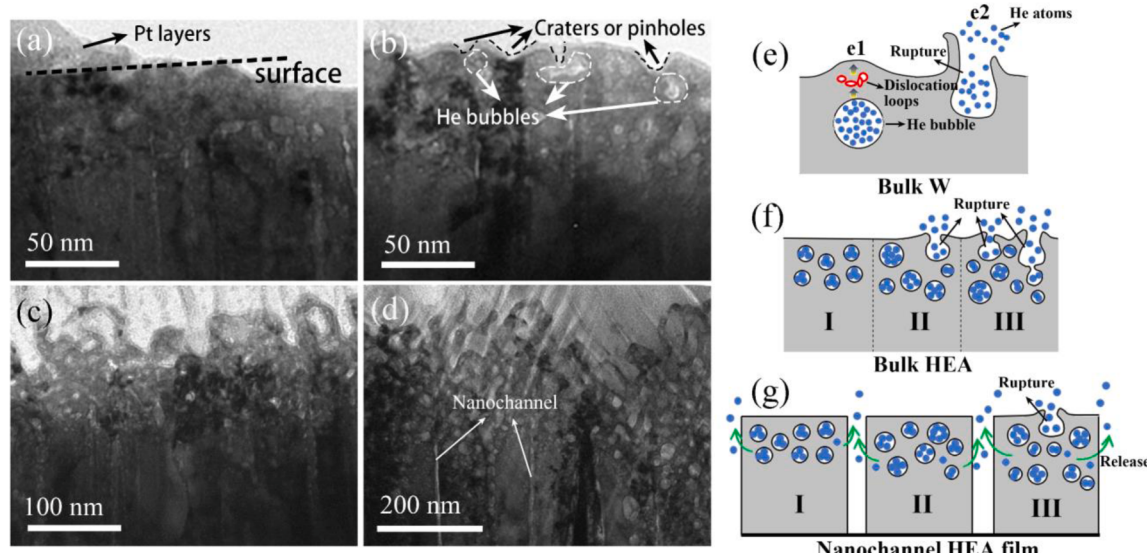


**Fig. 7.** Microstructure evolution and diagrammatic sketch of fuzz formation. Cross-sectional TEM images of the nanochannel HEA films irradiated to the fluences of (a)  $1 \times 10^{25}$ , (b)  $5 \times 10^{25}$ , (c)  $1 \times 10^{26}$ , (d)  $3 \times 10^{26}$  ions  $\text{m}^{-2}$ ; (e1) Protrusions and (e2) rupture of He bubble of the fuzz formation in (e) the bulk W; Diagrammatic sketch of the microcosmic process of He bubble bursting to form fuzz in the (f) bulk HEA and (g) nanochannel HEA film.

factors in effectively reducing the growth rate of the fuzz in the nanochannel HEA film. Thus, the effective nanostructure design further increases the performance of HEA. It should be noted that the introducing GB into materials is a good strategy to enhance radiation resistance [10, 11]. However, this is not the case of this study. As shown in Fig. 1, the growth character of columnar grains by magnetron sputtering deposition determined that a columnar grain is in single crystal structure.

## 5. Conclusions

In summary, a new plasma-facing material of single-phase nanochannel CrMoTaWV HEA film was prepared. Under the low-energy and

high-flux He plasma exposure at 1270 K, the HEA not only exhibits 20 times higher formation fluence of fuzz structure than that of W, but also has a remarkable 8.9 times slower growth rate of fuzz. *In-situ* TEM observation and TDS results show that the diffusion of He atoms and the growth of He bubbles in the nanochannel HEA film are much slower than those in W. The MD simulations shows that the self-interstitial atoms induced by He bubble growth in the HEA do not emit to the surface but migrate around in a non-directional way due to the surrounding complex atom environment, differing from the W atoms that are emitted to the surface to form protuberances. Compared to traditional metal, there is an unusual interaction between HEA and He: the SIAs induced by the growth of He bubble in HEA distribute around the

bubble in a non-directional way rather than being emitted directionally in the form of dislocation loops as in W. Meanwhile, HEA effectively hinders the growth and coalescence of He bubbles to form large ones. Therefore, the growth of fuzz in HEA under He plasma irradiation is slowed down. Compared to the bulk HEA, the nanochannel structure further enhances the irradiation resistance because the free surfaces of nanochannels release He atoms outside of matrix. The results clearly reveal that the nanochannel structural HEA material is a new kind of promising plasma-facing materials and nuclear structural materials.

### Declaration of Competing Interest

The authors declare that they have no known competing financial interests or personal relationships that could have appeared to influence the work reported in this paper.

### Acknowledgments

This work was supported by the National Natural Science Foundation of China (grants 12275197, 12105206, and 11935011), the Natural Science Foundation of Hubei Province, China (grants 2020CFA041), the SPC-Lab Research Fund (WDZC202001) and the Fundamental Research Funds for the Central Universities (2042022kf1184) for financial support. This work was performed, in part, at the Center for Integrated Nanotechnologies, an Office of Science User Facility operated for the U. S. Department of Energy (DOE) Office of Science. Los Alamos National Laboratory, an affirmative action equal opportunity employer, is managed by Triad National Security, LLC for the U.S. Department of Energy's NNSA, under contract 89233218CNA000001. The numerical calculations in this paper have been done on the supercomputing system in the Supercomputing Center of Wuhan University.

### Supplementary materials

Supplementary material associated with this article can be found, in the online version, at doi:[10.1016/j.actamat.2023.118765](https://doi.org/10.1016/j.actamat.2023.118765).

### References

- [1] W. Qin, Y. Wang, M. Tang, F. Ren, Q. Fu, G. Cai, L. Dong, L. Hu, G. Wei, C. Jiang, Microstructure and hardness evolution of nanochannel W films irradiated by helium at high temperature, *J. Nucl. Mater.* 502 (2018) 132–140.
- [2] Z. Zhang, E. Hasenhuettl, K. Yabuuchi, A. Kimura, Evaluation of helium effect on ion-irradiation hardening in pure tungsten by nano-indentation method, *Nucl. Mater. Energy* 9 (2016) 539–546.
- [3] J. Knaster, A. Moeslang, T. Muroga, Materials research for fusion, *Nat. Phys.* 12 (5) (2016) 424–434.
- [4] A. Hakola, J. Likonen, A. Lahtinen, T. Vuoriheimo, M. Groth, H. Kumpulainen, M. Balden, K. Krieger, M. Mayer, T. Schwarz-Selinger, S. Brezinsek, M. Kelemen, S. Markelj, M. Barac, S. Gouasmia, I. Bogdanovic Radovic, A. Uccello, E. Vassallo, D. Dellasega, M. Passoni, M. Sala, E. Bernard, M. Diez, C. Guillemaut, E. Tsitrone, the ASDEX Upgrade Team, the EUROfusion MST1 Team, the EUROfusion WP PFC Contributors, Gross and net erosion balance of plasma-facing materials in full-W tokamaks, *Nucl. Fusion* 61 (11) (2021), 116006.
- [5] M. Firdauss, Q. Li, M. Lipa, G. Luo, M. Missirlian, M. Richou, W. Wang, First feedback during series fabrication of ITER like divertor tungsten components for the WEST tokamak, *Phys. Scr.* 96 (12) (2021), 124037.
- [6] M. Gago, A. Kreter, B. Unterberg, M. Wirtz, Synergistic and separate effects of plasma and transient heat loads on the microstructure and physical properties of ITER-grade tungsten, *Phys. Scr.* 96 (12) (2021), 124052.
- [7] R.A. Pitts, S. Carpenter, F. Escourbiac, T. Hirai, V. Komarov, S. Liso, A. S. Kukushkin, A. Loarte, M. Merola, A. Sashala Naik, R. Mitteau, M. Sugihara, B. Bazylev, P.C. Stangeby, A full tungsten divertor for ITER: physics issues and design status, *J. Nucl. Mater.* 438 (2013) S48–S56.
- [8] J. Wang, D. Liu, Z. Guo, B. He, W. Dang, Molecular dynamics study on the origin of fuzz structure on tungsten surface, *J. Nucl. Mater.* 547 (2021), 152835.
- [9] S. Kajita, T. Morgan, H. Tanaka, Y. Hayashi, N. Yoshida, D. Nagata, J. Vernimmen, S. Feng, R. Zhang, N. Ohno, Accelerated/reduced growth of tungsten fuzz by deposition of metals, *J. Nucl. Mater.* 548 (2021), 152844.
- [10] O. El-Atwani, K. Hattar, J.A. Hinks, G. Greaves, S.S. Harilal, A. Hassanein, Helium bubble formation in ultrafine and nanocrystalline tungsten under different extreme conditions, *J. Nucl. Mater.* 458 (2015) 216–223.
- [11] O. El-Atwani, S. Gonderman, M. Efe, G. De Temmerman, T. Morgan, K. Bystrov, D. Klenosky, T. Qiu, J.P. Allain, Ultrafine tungsten as a plasma-facing component in fusion devices: effect of high flux, high fluence low energy helium irradiation, *Nucl. Fusion* 54 (8) (2014), 083013.
- [12] G. Duan, X. Li, J. Sun, C. Hao, Y. Xu, Y. Zhang, W. Liu, C.S. Liu, Surface-structure dependence of healing radiation-damage mechanism in nanoporous tungsten, *J. Nucl. Mater.* 498 (2018) 362–372.
- [13] W. Qin, F. Ren, R.P. Doerner, G. Wei, Y. Lv, S. Chang, M. Tang, H. Deng, C. Jiang, Y. Wang, Nanochannel structures in W enhance radiation tolerance, *Acta Mater.* 153 (2018) 147–155.
- [14] A. Hasegawa, M. Fukuda, K. Yabuuchi, S. Nogami, Neutron irradiation effects on the microstructural development of tungsten and tungsten alloys, *J. Nucl. Mater.* 471 (2016) 175–183.
- [15] H. Jo, S. Park, D. You, S. Kim, D. Lee, Combinatorial discovery of irradiation damage tolerant nano-structured W-based alloys, *J. Nucl. Mater.* 572 (2022), 154066.
- [16] Z. Cao, M. Pan, K. Hu, Z. Huang, Y. Lv, S. Wen, Y. Zhao, H. Deng, Effect of titanium on the precipitation behaviors of transmutation elements in tungsten-titanium alloys from first-principles calculations, *Fusion Eng. Des.* 158 (2020), 111673.
- [17] A. Richter, W. Anwand, C.L. Chen, R. Böttger, Evaluation of defect formation in helium irradiated  $\text{Y}_2\text{O}_3$  doped W-Ti alloys by positron annihilation and nanoindentation, *J. Nucl. Mater.* 494 (2017) 294–302.
- [18] S. Gonderman, J.K. Tripathi, T.J. Novakowski, T. Sizyuk, A. Hassanein, The effect of low energy helium ion irradiation on tungsten-tantalum (W-Ta) alloys under fusion relevant conditions, *J. Nucl. Mater.* 491 (2017) 199–205.
- [19] Y. Zayachuk, M.H.J. t Hoen, P.A. Zeijlmans van Emmichoven, D. Terentyev, I. Uytendhouwen, G. van Oost, Surface modification of tungsten and tungsten-tantalum alloys exposed to high-flux deuterium plasma and its impact on deuterium retention, *Nucl. Fusion* 53 (1) (2013), 013013.
- [20] K. Huang, L.M. Luo, X. Zan, Q. Xu, D.G. Liu, X.Y. Zhu, J.G. Cheng, Y.C. Wu, Microstructure and damage behavior of W-Cr alloy under He irradiation, *J. Nucl. Mater.* 501 (2018) 181–188.
- [21] J. Yan, X. Li, Z. Wang, K. Zhu, Comparison of surface morphologies and helium retention of nanocrystalline W and W-Cr films prepared by magnetron sputtering, *Nucl. Mater. Energy* 22 (2020), 100733.
- [22] A. Poulia, E. Georgatis, A. Lekatou, A. Karantzalis, Dry-sliding wear response of MoTaWNbV high entropy alloy, *Adv. Eng. Mater.* 19 (2) (2017), 1600535.
- [23] Y. Long, X. Liang, K. Su, H. Peng, X. Li, A fine-grained NbMoTaWCr refractory high-entropy alloy with ultra-high strength: microstructural evolution and mechanical properties, *J. Alloy. Compd.* 780 (2019) 607–617.
- [24] Z. Lei, X. Liu, Y. Wu, H. Wang, S. Jiang, S. Wang, X. Hui, Y. Wu, B. Gault, P. Kontis, D. Raabe, L. Gu, Q. Zhang, H. Chen, H. Wang, J. Liu, K. An, Q. Zeng, T.G. Nieh, Z. Lu, Enhanced strength and ductility in a high-entropy alloy via ordered oxygen complexes, *Nature* 563 (7732) (2018) 546–550.
- [25] B. Chen, S. Li, H. Zong, X. Ding, J. Sun, E. Ma, Unusual activated processes controlling dislocation motion in body-centered-cubic high-entropy alloys, *Proc. Natl. Acad. Sci. USA* 117 (28) (2020) 16199–16206.
- [26] Y. Bu, Y. Wu, Z. Lei, X. Yuan, H. Wu, X. Feng, J. Liu, J. Ding, Y. Lu, H. Wang, Z. Lu, W. Yang, Local chemical fluctuation mediated ductility in body-centered-cubic high-entropy alloys, *Mater. Today* 46 (2021) 28–34.
- [27] W. Zhang, P.K. Liaw, Y. Zhang, Science and technology in high-entropy alloys, *Sci. China Mater.* 61 (1) (2018) 2–22.
- [28] C. Lee, Y. Chou, G. Kim, M.C. Gao, K. An, J. Brechtl, C. Zhang, W. Chen, J. Poplawsky, G. Song, Y. Ren, Y.C. Chou, P.K. Liaw, Lattice-distortion-enhanced yield strength in a refractory high-entropy alloy, *Adv. Mater.* 32 (49) (2020), e2004029.
- [29] R.K. Nutor, Q. Cao, X. Wang, D. Zhang, Y. Fang, Y. Zhang, J.Z. Jiang, Phase selection, lattice distortions, and mechanical properties in high-entropy alloys, *Adv. Eng. Mater.* 22 (11) (2020), 2000466.
- [30] S. Alvi, F. Akhtar, High temperature tribology of CuMoTaWV high entropy alloy, *Wear* 426–427 (2019) 412–419.
- [31] D.B. Miracle, High-entropy alloys: a current evaluation of founding ideas and core effects and exploring “nonlinear” alloys, *JOM* 69 (11) (2017) 2130–2136.
- [32] E. Lu, J. Zhao, I. Makkonen, K. Mizohata, Z. Li, M. Hua, F. Djurabekova, F. Tuomisto, Enhancement of vacancy diffusion by C and N interstitials in the equiatomic FeMnNiCoCr high entropy alloy, *Acta Mater.* 215 (2021), 117093.
- [33] T. Yang, W. Guo, J.D. Poplawsky, D. Li, L. Wang, Y. Li, W. Hu, M.L. Crespillo, Z. Yan, Y. Zhang, Y. Wang, S.J. Zinkle, Structural damage and phase stability of Al<sub>10</sub>Cr<sub>3</sub>Co<sub>6</sub>Fe<sub>11</sub> high entropy alloy under high temperature ion irradiation, *Acta Mater.* 188 (2020) 1–15.
- [34] O. El-Atwani, N. Li, M. Li, A. Devaraj, E. Martinez, Outstanding radiation resistance of tungsten-based high entropy alloys, *Sci. Adv.* 5 (3) (2019) eaav2002.
- [35] C. Lu, L. Niu, N. Chen, K. Jin, T. Yang, P. Xiu, Y. Zhang, F. Gao, H. Bei, S. Shi, M. R. He, I.M. Robertson, W.J. Weber, L. Wang, Enhancing radiation tolerance by controlling defect mobility and migration pathways in multicomponent single-phase alloys, *Nat. Commun.* 7 (2016) 13564.
- [36] D. Chen, Y. Tong, H. Li, J. Wang, Y.L. Zhao, A. Hu, J.J. Kai, Helium accumulation and bubble formation in FeCoNiCr alloy under high fluence He<sup>+</sup> implantation, *J. Nucl. Mater.* 501 (2018) 208–216.
- [37] Q. Yang, Y.W. You, L. Liu, H. Fan, W. Ni, D. Liu, C.S. Liu, G. Benstetter, Y. Wang, Nanostructured fuzz growth on tungsten under low-energy and high-flux He irradiation, *Sci. Rep.* 5 (2015) 10959.
- [38] M. Huang, Y. Li, G. Ran, Z. Yang, P. Wang, Cr-coated Zr-4 alloy prepared by electroplating and its *in situ* He<sup>+</sup> irradiation behavior, *J. Nucl. Mater.* 538 (2020), 152240.
- [39] P. Zhao, X. Guan, H. Zheng, S. Jia, L. Li, H. Liu, L. Zhao, H. Sheng, W. Meng, Y. Zhuang, J. Wu, L. Li, J. Wang, Surface- and strain-mediated reversible phase

- transformation in quantum-confined ZnO nanowires, *Phys. Rev. Lett.* 123 (21) (2019), 216101.
- [40] T. Malis, S.C. Cheng, R.F. Egerton, EELS log-ratio technique for specimen-thickness measurement in the TEM, *J. Electron Microsc. Tech.* 8 (1988) 193–200.
- [41] C.H.M. Broeders, A.Y. Konobeyev, Defect production efficiency in metals under neutron irradiation, *J. Nucl. Mater.* 328 (2–3) (2004) 197–214.
- [42] S.J. Plimpton, Fast parallel algorithms for short-range molecular dynamics, *J. Comput. Phys.* 117 (1995) 1–19.
- [43] X.W. Zhou, R.A. Johnson, H.N.G. Wadley, Misfit-energy-increasing dislocations in vapor-deposited CoFe/NiFe multilayers, *Phys. Rev. B* 69 (14) (2004), 144113.
- [44] S. Zhao, Y. Xiong, S. Ma, J. Zhang, B. Xu, J.J. Kai, Defect accumulation and evolution in refractory multi-principal element alloys, *Acta Mater.* 219 (2021), 117233.
- [45] E. Antillon, C. Woodward, S.I. Rao, B. Akdim, T.A. Parthasarathy, Chemical short range order strengthening in a model FCC high entropy alloy, *Acta Mater.* 190 (2020) 29–42.
- [46] E. Antillon, C. Woodward, S.I. Rao, B. Akdim, Chemical short range order strengthening in BCC complex concentrated alloys, *Acta Mater.* 215 (2021), 117012.
- [47] Z. Lin, R.A. Johnson, L.V. Zhigilei, Computational study of the generation of crystal defects in a bcc metal target irradiated by short laser pulses, *Phys. Rev. B* 77 (21) (2008), 214108.
- [48] D.E. Beck, A new interatomic potential function for helium, *Mol. Phys.* 14 (4) (1968) 311–315.
- [49] S. Liu, L. Xie, Q. Peng, R. Li, Carbon nanotubes enhance the radiation resistance of bcc iron revealed by atomistic study, *Materials* 12 (2) (2019) 217 (Basel).
- [50] M.J. Baldwin, R.P. Doerner, Helium induced nanoscopic morphology on tungsten under fusion relevant plasma conditions, *Nucl. Fusion* 48 (3) (2008), 035001.
- [51] L. Liu, S. Li, D. Liu, G. Benstetter, Y. Zhang, Y. Hong, H. Fan, W. Ni, Q. Yang, Y. Wu, Z. Bi, Surface damages of polycrystalline W and La<sub>2</sub>O<sub>3</sub>-doped W induced by high-flux He plasma irradiation, *J. Nucl. Mater.* 501 (2018) 275–281.
- [52] T.J. Petty, M.J. Baldwin, M.I. Hasan, R.P. Doerner, J.W. Bradley, Tungsten ‘fuzz’ growth re-examined: the dependence on ion fluence in non-erosive and erosive helium plasma, *Nucl. Fusion* 55 (9) (2015), 093033.
- [53] G. De Temmerman, T. Hirai, R. Pitts, The influence of plasma-surface interaction on the performance of tungsten at the ITER divertor vertical targets, *Plasma Phys. Control. Fusion* 60 (4) (2018), 044018.
- [54] J.A. Wright, A review of late-stage tungsten fuzz growth, *Tungsten* 4 (3) (2022) 184–193.
- [55] D. Nishijima, M. Baldwin, R. Doerner, J. Yu, Sputtering properties of tungsten ‘fuzzy’ surfaces, *J. Nucl. Mater.* 415 (1) (2011) S96–S99.
- [56] G. De Temmerman, R. Doerner, R. Pitts, A growth/annealing equilibrium model for helium-induced nanostructure with application to ITER, *Nucl. Mater. Energy* 19 (2019) 255–261.
- [57] R. Kobayashi, T. Hattori, T. Tamura, S. Ogata, A molecular dynamics study on bubble growth in tungsten under helium irradiation, *J. Nucl. Mater.* 463 (2015) 1071–1074.
- [58] J. Zhan, T. Okita, M. Ye, D. Kato, K. Suzuki, Simulation study of helium bubble coalescence in tungsten at various temperatures relevant to fusion conditions, *Comput. Mater. Sci.* 187 (2021), 110076.
- [59] F. Sefta, K.D. Hammond, N. Juslin, B.D. Wirth, Tungsten surface evolution by helium bubble nucleation, growth and rupture, *Nucl. Fusion* 53 (7) (2013), 073015.
- [60] H. Schroeder, P.F. Fichtner, On the coarsening mechanisms of helium bubbles-Ostwald ripening versus migration and coalescence, *J. Nucl. Mater.* 179 (1991) 1007–1010.
- [61] C. Lu, T. Yang, K. Jin, N. Gao, P. Xiu, Y. Zhang, F. Gao, H. Bei, W.J. Weber, K. Sun, Y. Dong, L. Wang, Radiation-induced segregation on defect clusters in single-phase concentrated solid-solution alloys, *Acta Mater.* 127 (2017) 98–107.
- [62] O. El-Atwani, A. Alvarado, K. Unal, S. Fensin, J.A. Hinks, G. Greaves, J.K. Baldwin, S.A. Maloy, E. Martinez, Helium implantation damage resistance in nanocrystalline W-Ta-V-Cr high entropy alloys, *Mater. Today Energy* 19 (2021), 100599.
- [63] W. Qin, F. Ren, J. Zhang, X. Dong, Y. Feng, H. Wang, J. Tang, G. Cai, Y. Wang, C. Jiang, Helium retention in krypton ion pre-irradiated nanochannel W film, *Nucl. Fusion* 58 (2) (2018), 026021.
- [64] Q. Xu, J. Zhang, K. Maejima, N. Hirashita, Retention and thermal desorption of helium in pure tungsten, *Philos. Mag. Lett.* 96 (12) (2016) 477–481.
- [65] A.M. Ito, A. Takayama, Y. Oda, T. Tamura, R. Kobayashi, T. Hattori, S. Ogata, N. Ohno, S. Kajita, M. Yajima, Y. Noiri, Y. Yoshimoto, S. Saito, S. Takamura, T. Murashima, M. Miyamoto, H. Nakamura, Molecular dynamics and Monte Carlo hybrid simulation for fuzzy tungsten nanostructure formation, *Nucl. Fusion* 55 (7) (2015), 073013.
- [66] C.S. Chen, D. Dasgupta, R.D. Kolasinski, B.D. Wirth, D. Maroudas, Onset of fuzz formation in plasma-facing tungsten as a surface morphological instability, *Phys. Rev. Mater.* 5 (11) (2021), 113403.
- [67] W.W. Zhang, P.H. Shi, B.D. Yao, L. Wu, X.Y. Wu, L.Q. Shi, Y.X. Wang, Panorama of “fuzz” growth on tungsten surface under He irradiation, *Appl. Surf. Sci.* 542 (2021), 148543.